J. Fluid Mech. (2024), *vol*. 984, A51, doi:10.1017/jfm.2024.258

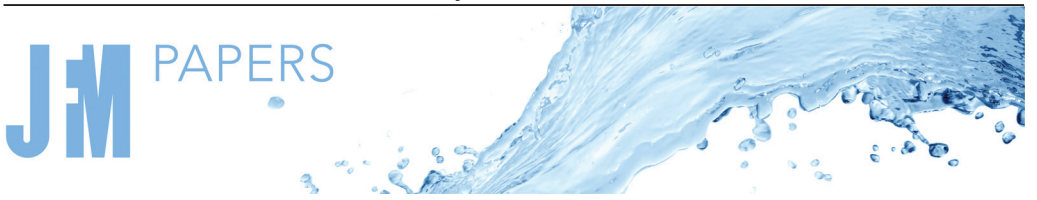

Flow-induced vibrations with and without structural restoring force: convergence under the effect of path curvature

Rémi Bourguet†

Institut de Mécanique des Fluides de Toulouse, Université de Toulouse and CNRS, Toulouse 31400, France

(Received 19 December 2023; revised 5 March 2024; accepted 10 March 2024)

When a cylinder is free to move along a transverse rectilinear path within a current, the vibrations developing with and without structural restoring force (SRF) noticeably deviate: if the elastic support is removed, their onset is delayed from a Reynolds number (Re, based on the body diameter and inflow velocity) value of approximately 20 to 30, and their peak amplitudes and frequency bandwidths are substantially reduced. The present study examines the influence of a curved path on this deviation by considering that the cylinder, mounted on an elastic support or not, is free to translate along a circular path whose radius is varied. The investigation is carried out numerically at $Re = 25$ and 100, i.e. subcritical and postcritical values relative to the threshold of 47 that marks the onset of flow unsteadiness for a fixed body. The principal result of this work is that the behaviours of the flow–structure systems with and without SRF tend to converge under the effect of path curvature. Beyond a certain curvature magnitude, both systems explore the same vibration ranges and the presence or absence of SRF becomes indiscernible. This convergence is accompanied by an enhancement of the responses appearing without SRF. It is analysed in light of the evolution of the effective added mass which determines the subset of responses reached with SRF that remain accessible without SRF. The apparent continuity of the physical mechanisms between the subcritical- and postcritical-Re values suggests that the convergence phenomenon uncovered here could persist at higher Re.

Key words: flow–structure interactions, vortex streets, wakes

1. Introduction

In nature and in industrial systems, the flow-induced vibrations (FIV) of bluff bodies are frequently encountered in physical configurations that involve a structural restoring force

† Email address for correspondence: remi.bourguet@imft.fr

(SRF) and thus a structural natural frequency (Païdoussis, Price & de Langre 2010). This is in particular the case of vortex-induced vibrations (VIV), a form of FIV which develops through synchronization between body motion and flow unsteadiness. As a result, in the canonical problem employed to study VIV, i.e. a circular cylinder free to translate along a rectilinear path in the direction normal to the current, the body is usually mounted on an elastic support (Williamson & Govardhan 2004). Yet, VIV still occur when the elastic support and associated SRF are removed, including at Reynolds number (Re, based on the body diameter and inflow velocity) values lower than the critical threshold of 47 that marks the onset of flow unsteadiness for a fixed cylinder (Shiels, Leonard & Roshko 2001; Govardhan & Williamson 2002; Ryan, Thompson & Hourigan 2005; Navrose & Mittal 2017; Bourguet 2023*a*).

The vibrations appearing in the above canonical problem without SRF deviate from those typically reported with SRF: their onset is delayed from $Re \approx 20$ to $Re \approx 30$, and they only exhibit substantial magnitudes over a narrow range of low values of the structure to displaced fluid mass ratio, with lower peak amplitudes. The deviation between the responses with and without SRF can be analysed under a harmonic oscillation assumption, which is often acceptable in this context (Govardhan & Williamson 2002). This analysis shows that the responses accessible without SRF correspond to the subset of those occurring with SRF where the effective added mass due to fluid forcing is negative. Along a rectilinear path, this subset does not include the peak amplitude responses observed with SRF, which are characterized by positive added mass values (e.g. Hover, Techet & Triantafyllou 1998), and it may even vanish, depending on Re.

The present work was motivated by two recent studies concerning a cylinder immersed in a current and free to translate along a circular arc, with and without SRF (Bourguet 2023*a*,*b*). Path curvature induces a global enhancement of the responses developing without SRF. Among other aspects, it causes a reduction of the critical value of Re for the onset of vibrations/flow unsteadiness, and an amplification of the responses, which tend to be comparable to those observed with SRF. The increasing trend of the response frequency with path curvature magnitude, identified with SRF, suggests a reduction of the effective added mass, which may become negative for most of the vibrations of substantial amplitudes. These responses could thus be reached without SRF. The possible convergence of the behaviours of the systems with and without SRF, under the effect of path curvature, is the object of this work. In order to explore this convergence, the systems with and without SRF are considered over a range of circular path radii, including the limiting case where the radius tends to infinity, i.e. the rectilinear path configuration. The investigation is based on numerical simulations at $Re = 25$, a subcritical value for which rectilinear vibrations arise with SRF (Cossu & Morino 2000; Kou *et al.* 2017; Dolci & Carmo 2019) but not without SRF (Bourguet 2023*a*), and $Re = 100$, the postcritical value selected in the above-mentioned prior studies on this topic.

2. Physical configuration and numerical method

A sketch of the physical configuration is presented in figure 1(*a*). The circular cylinder of diameter D and mass per unit length M_c is parallel to the z axis and placed in an incompressible uniform current of velocity U, density ρ_f, viscosity μ, aligned with the x axis. The Reynolds number, $Re = \rho_f UD/\mu$, is kept below or equal to 100. The flow is two-dimensional across the parameter space investigated. This point has been verified via three-dimensional simulations. The two-dimensional Navier–Stokes equations are employed to predict the flow dynamics. The cylinder is free to translate along a circular path of radius R, parallel to the (x, y) plane and centred at the origin of the

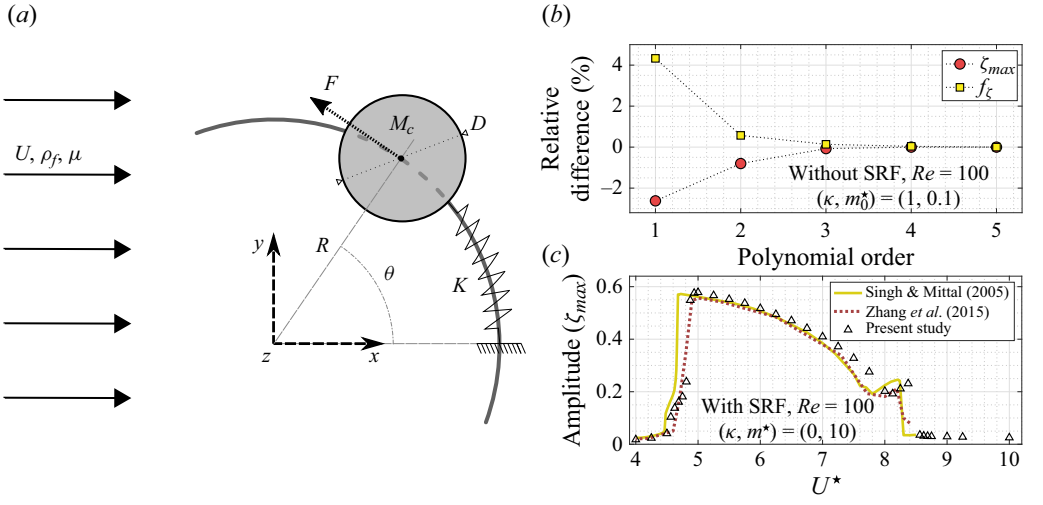

Figure 1. (*a*) Sketch of the physical configuration. (*b*) Relative differences of the displacement amplitude (ζ_{max}) and frequency (f_ζ) with respect to the fifth-order simulation results, as functions of the polynomial order, without SRF at $Re = 100$, for $\kappa = 1$ and $m_0^\star = 0.1$. (*c*) Rectilinear displacement amplitude with SRF as a function of $U^\star$, at $Re = 100$ for $m^\star = 10$; the present results are compared with those reported by Singh & Mittal (2005) and Zhang *et al.* (2015).

(x, y, z) frame. The stiffness of the elastic support is denoted by K; it is set to zero when the SRF is removed. The cylinder position is tracked by the angle θ relative to the x axis. The physical variables are non-dimensionalized by D, U and ρ_f. The non-dimensional curvilinear displacement of the body along the circular path is $\zeta = \theta/\kappa$, where $\kappa = D/R$ is the non-dimensional curvature magnitude. The limiting case where R tends to infinity ($\kappa = 0$) corresponds to the transverse rectilinear motion configuration, where ζ is the non-dimensional displacement aligned with the y axis. The in-line, transverse and tangential force coefficients are defined as $\{C_x, C_y, C\} = 2\{F_x, F_y, F\}/(\rho_f D U^2)$, where F_x, F_y and F are the dimensional fluid forces per unit length, parallel to the x and y axes, and to the direction of body motion, respectively. The motion of the cylinder is governed by the following equation:

$$\ddot{\zeta} + (2\pi f_n)^2\,\zeta = \frac{2C}{\pi m^\star}, \quad \text{with } C = -C_x \sin(\kappa\zeta) + C_y \cos(\kappa\zeta). \tag{2.1}$$

The $\dot{}$ symbol designates the non-dimensional time derivative. The structure to displaced fluid mass ratio, the non-dimensional natural frequency and associated reduced velocity are defined as $m^\star = 4M_c/(\pi\rho_f D^2)$, $f_n = D/(2\pi U)\sqrt{K/M_c}$ and $U^\star = 1/f_n$, respectively. In the absence of SRF ($f_n = 0$), the mass ratio is denoted by $m_0^\star$. No structural damping is included but the analysis presented hereafter also applies to damped systems.

Considering a harmonic response at frequency f_ζ, the dynamics equation (2.1) indicates that the same behaviour can be observed with and without SRF, i.e. for $f_n > 0$ and $f_n = 0$, when

$$m_0^\star = m^\star\left[1 - \left(\frac{f_n}{f_\zeta}\right)^2\right] = -C_m, \tag{2.2}$$

where C_m is the effective added mass coefficient. Without SRF, the condition $m_0^\star > 0$ implies that C_m is negative, as also noted by Govardhan & Williamson (2002).

Therefore, only a part of the responses reached with SRF can be attained without SRF: the responses where $C_m < 0$, or equivalently $f_\zeta > f_n$. The actual vibrations are often close to sinusoidal and (2.2) will be used to explore the connection between the responses arising with and without SRF, in particular the evolution of the response range accessible without SRF as κ is varied.

A quasi-steady model of C and its first-order approximation about $\zeta = \dot{\zeta} = 0$ can be expressed as follows (Bourguet 2023*b*):

$$C^{qs} = -\bar{C}_x^f(\dot{\zeta} + \sin(\kappa\zeta))\sqrt{\dot{\zeta}^2 + 2\dot{\zeta}\sin(\kappa\zeta) + 1} \approx -\bar{C}_x^f(\dot{\zeta} + \kappa\zeta), \tag{2.3}$$

where $\bar{C}_x^f$ is the mean in-line force (or drag) coefficient in the fixed body case. The $\bar{}$ symbol denotes the time-averaged value. The term relative to ζ in the C^{qs} approximation is used to derive a modified natural frequency

$$f_n' = \sqrt{f_n^2 + \frac{\bar{C}_x^f \kappa}{2\pi^3 m^\star}}. \tag{2.4}$$

The system behaviour generally departs from the quasi-steady assumption, i.e. decoupling of the flow and moving body time scales. Yet, f_n' was shown to be significant, especially without SRF ($f_n = 0$), as it determines the location of the vibration region in the $(\kappa, m_0^\star)$ parameter space (Bourguet 2023*a*). Assuming that a peak of vibration occurs close to f_n' when this frequency coincides with the Strouhal frequency (St, frequency of flow unsteadiness for a fixed body), (2.4) indicates that the peak encountered with SRF should (i) shift towards higher $U^\star$ values, and (ii) involve higher frequencies relative to f_n, as κ is increased. This suggests a decreasing trend of C_m (2.2) and thus an expansion of the response range accessible without SRF. These conjectures are examined in the next section on the basis of numerical simulations.

The numerical method is the same as in previous studies concerning comparable systems (Bourguet 2023*a*,*b*). It is briefly summarized and some additional convergence/validation results are presented. The coupled flow–structure equations are solved by the parallelized code *Nektar*, which is based on the spectral/*hp* element method (Karniadakis & Sherwin 1999). Body motion is taken into account by adding inertial terms in the Navier–Stokes equations (Newman & Karniadakis 1997). The large rectangular computational domain (350D downstream and 250D in front, above and below the cylinder) is discretized into 3975 spectral elements. A no-slip condition is applied on the cylinder surface. The free-stream value is assigned for the velocity at the upstream boundary. At the downstream boundary, a Neumann-type boundary condition is used. Flow periodicity conditions are employed on the upper and lower boundaries.

Figure 1(*b*) depicts a convergence study in a typical case of curvilinear vibrations without SRF, at $Re = 100$. The evolutions of the relative differences with respect to the fifth-order simulation results, for the displacement amplitude and frequency (f_ζ), as functions of the spectral element polynomial order, show that an increase from order 4 to 5 has not impact on the results. Here, and in the following, $\bar{\zeta} = 0$ and the amplitude is measured as the maximum value of the displacement signal (ζ_{max}). A polynomial order of 4 was selected. A similar procedure was employed to set the non-dimensional time step to 0.0025. The rectilinear displacement amplitudes observed with SRF at $Re = 100$ are compared in figure 1(*c*) with those reported by Singh & Mittal (2005) and Zhang *et al.* (2015). This comparison confirms the validity of the present numerical method.

Each simulation is initialized with the established flow past a fixed body at the selected Re. Then, the body is released with an initial velocity $\dot{\zeta} = 0.1$. The analysis is based on time series collected after convergence, over 30 oscillation cycles in the unsteady cases.

3. Flow-induced vibrations with and without SRF

As a first step, focus is placed on the behaviour of the flow–structure system with SRF. The vibrations occurring at $Re = 25$ and $Re = 100$, i.e. subcritical and postcritical values of Re, are depicted in figures 2 and 3, which represent the displacement amplitude and frequency as functions of $U^\star$, for $m^\star = 10$. At each Re, the rectilinear path configuration ($\kappa = 0$) is considered first, then κ is progressively increased to visualize its influence on response properties. In all cases, the displacement amplitude exhibits a bell-shaped trend as a function of $U^\star$, which is typical of VIV. On each side of the bell-shaped curve, the flow–structure system reaches a steady state at $Re = 25$, while residual oscillations of low amplitudes persist at $Re = 100$. To facilitate the presentation, at $Re = 100$, the term 'vibration region' designates the $U^\star$ (or $-C_m$ in the following) range where $\zeta_{max} > 0.1$.

Body motion and flow unsteadiness are always synchronized at $Re = 25$, regardless of κ. This locked regime, which corresponds to the lock-in condition usually reported for VIV (Williamson & Govardhan 2004), also dominates at $Re = 100$. In addition, a desynchronized regime, called unlocked and enhanced by path curvature (Bourguet 2023*b*), may develop at this Re, near the edges of the vibration region. Despite the possible emergence of small higher-harmonic contributions and incommensurable components (at flow unsteadiness frequency in the unlocked regime), the vibrations remain close to sinusoidal in most cases. This justifies the application of the analysis introduced in § 2 (2.2) to link the responses arising with and without SRF. The value of C_m discussed hereafter is determined via (2.2). It is equal to the partial added mass coefficient associated with the spectral components of ζ and C at the dominant frequency of body displacement (f_ζ), and thus to the total added mass coefficient for sinusoidal oscillations. In figures 2 and 3, f_ζ is normalized by f_n and plotted together with the normalized values of f_n' and St. At $Re = 25$, the St value (0.105) is that obtained by Kou *et al.* (2017) by triggering the flow, and is $St = 0.164$ at $Re = 100$.

Along a rectilinear path ($\kappa = 0$), the structural responses occur below f_n for all $U^\star$ at $Re = 25$, and over a large portion of the vibration region, which includes the peak amplitude, at $Re = 100$. Equation (2.2) predicts that the responses where $f_\zeta > f_n$ ($C_m < 0$) can be attained without SRF, while those where $f_\zeta < f_n$ ($C_m > 0$) cannot be reached. The corresponding $U^\star$ ranges are indicated by yellow and grey background colours, respectively. As shown later in this section, these predictions are confirmed by the simulations carried out without SRF.

Within the vibration region, the ratio f_ζ/f_n tends to increase with κ. The proximity between f_ζ and f_n' suggests that this increasing trend is driven by the evolution of f_n', whose deviation from f_n is governed by the combined effects of the mean drag force and path curvature (2.4). The $U^\star$ range where $f_\zeta > f_n$ expands towards the lower limit of the vibration region, and crosses this limit, as κ is increased. According to (2.2), this signifies a progressive widening of the subset of responses accessible without SRF. For $\kappa = 2$ at $Re = 25$ and $\kappa = 5$ at $Re = 100$, this subset encompasses all the responses encountered in the vibration region.

Figure 4 represents the vibration region, as well as the areas of responses accessible and inaccessible without SRF, in the $(\kappa, U^\star)$ and $(\kappa, -C_m)$ domains, for each Re. It provides a global visualization of the expansion of the accessible response area, and of the simultaneous reduction of the inaccessible response area, within the vibration region, as κ

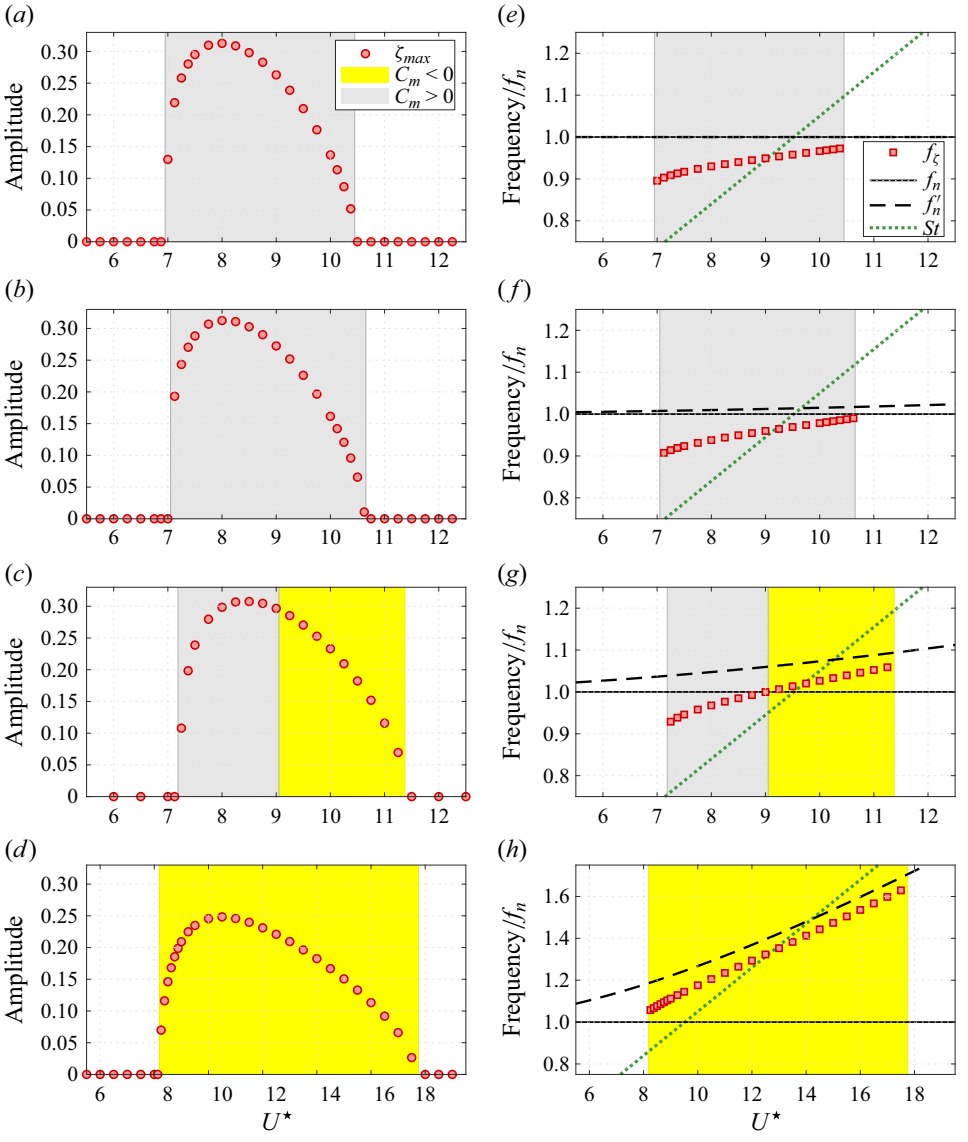

Figure 2. Displacement (*a–d*) amplitude and (*e–h*) frequency with SRF, as functions of $U^\star$ ($m^\star = 10$), at $Re = 25$, for (*a*,*e*) $\kappa = 0$, (*b*,*f*) $\kappa = 0.1$, (*c*,*g*) $\kappa = 0.5$ and (*d*,*h*) $\kappa = 2$. The displacement frequency is plotted together with the natural frequency, the modified natural frequency (2.4) and *St*; the frequency range is normalized by the natural frequency. Yellow and grey background colours denote the regions where $C_m < 0$ ($f_\zeta > f_n$) and $C_m > 0$ ($f_\zeta < f_n$), i.e. the regions of responses accessible and inaccessible without SRF, respectively.

is increased. This phenomenon corresponds to a regular translation of the vibration region along the effective added mass axis (figure 4*a* ii,*b* ii). The location of the peak amplitude (red dashed-dotted line) does not precisely coincide with $f_n' = St$ (figures 2 and 3), but it shifts towards higher $U^\star$ when κ is increased, as conjectured on the basis of (2.4). It can be noted that the peak amplitude enters the accessible response area for $\kappa \approx 0.7$, at both *Re* values. The similitude in the distribution of the accessible and inaccessible response areas relative to the vibration region, at $Re = 25$ and $Re = 100$, denotes a continuity of the physical mechanisms between the subcritical- and postcritical-*Re* ranges.

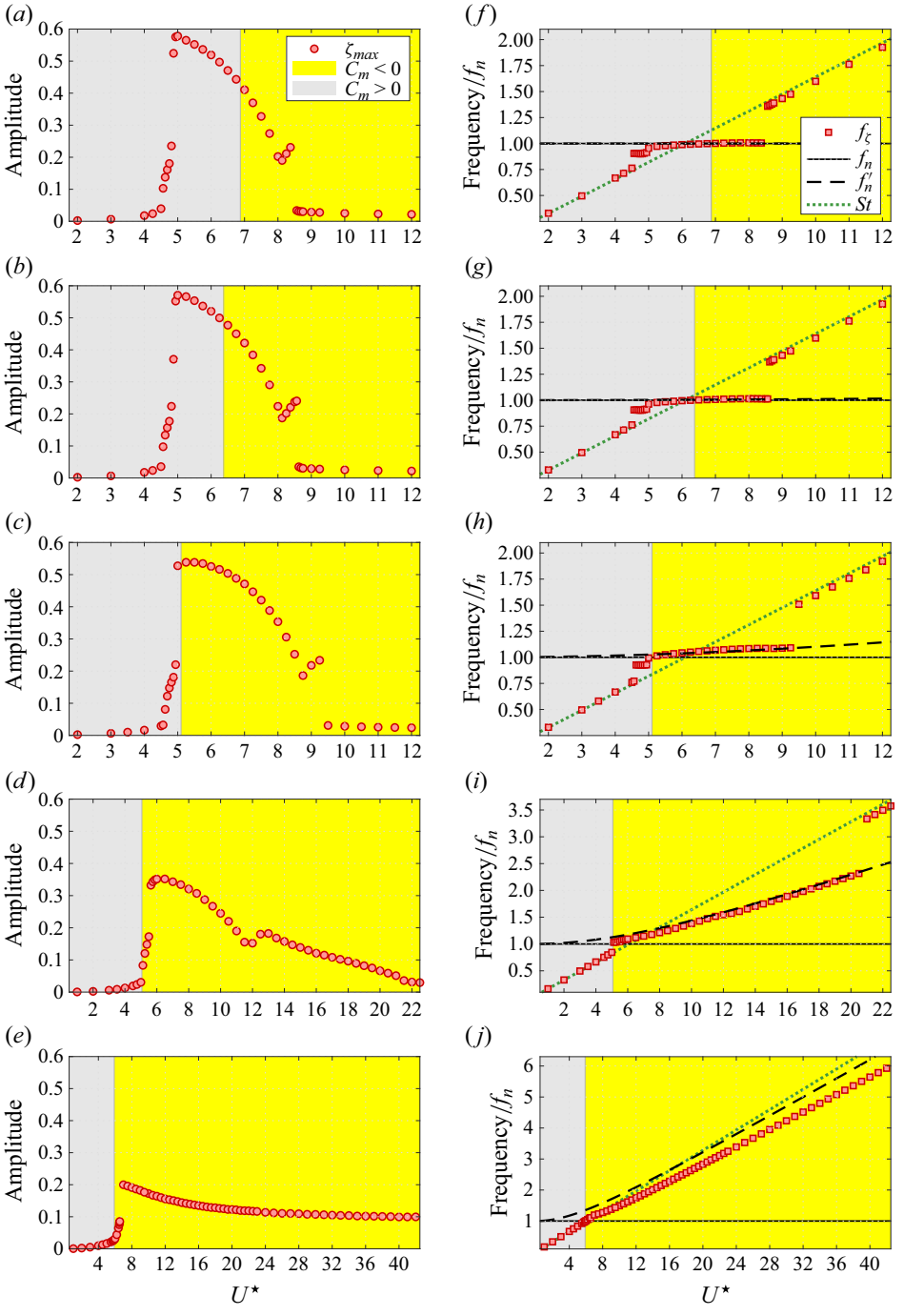

Figure 3. Same as figure 2 at $Re = 100$ for (a,f) $\kappa = 0$, (b,g) $\kappa = 0.1$, (c,h) $\kappa = 1$, (d,i) $\kappa = 5$ and (e,j) $\kappa = 11$.

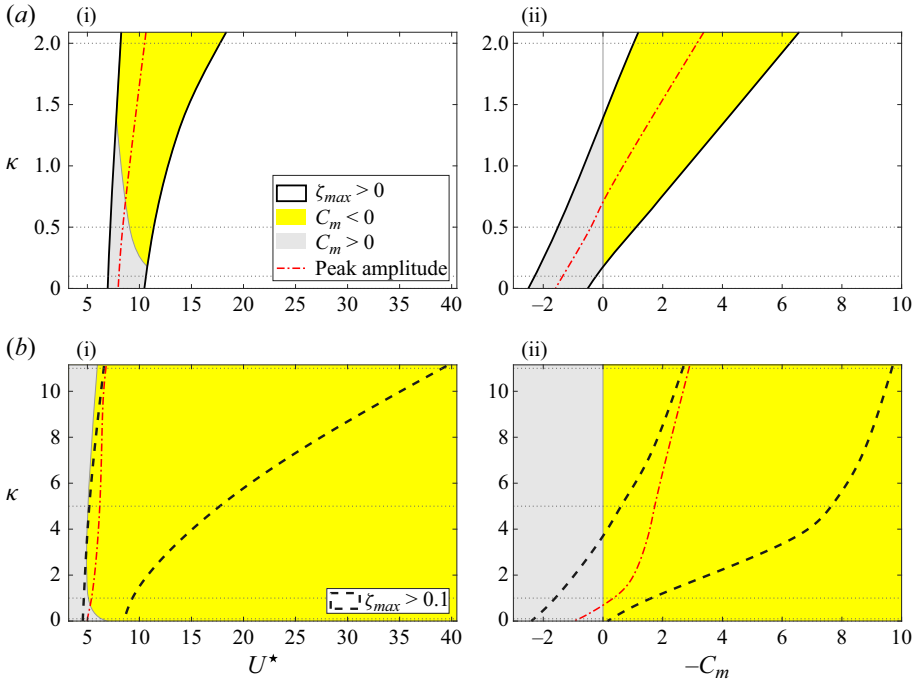

Figure 4. Vibration region with SRF in the (κ, $U^\star$) domain (*a* i,*b* i), and in the (κ, $-C_m$) domain (*a* ii,*b* ii), at (*a*) $Re = 25$ and (*b*) $Re = 100$. Black solid and dashed lines delimit the areas where $\zeta_{max} > 0$ in (*a*) and $\zeta_{max} > 0.1$ in (*b*). Yellow and grey background colours denote the regions where $C_m < 0$ ($f_\zeta > f_n$) and $C_m > 0$ ($f_\zeta < f_n$), i.e. the regions of responses accessible and inaccessible without SRF, respectively. A red dashed-dotted line locates the value of $U^\star$ or $-C_m$ where the peak amplitude is reached. Grey dotted lines indicate the cases visualized in figures 2, 3, 5 and 6.

In order to compare the responses of the systems with and without SRF, the displacement amplitudes and frequencies measured in both cases are plotted as functions of $-C_m$ in figures 5 ($Re = 25$) and 6 ($Re = 100$). The values of κ are the same as in figures 2 and 3. It is recalled that C_m is determined via (2.2) and thus $-C_m = m_0^\star$ in the absence of SRF; here, $m_0^\star$ ranges from 0.05 to 10 while $m^\star = 10$. These plots further illustrate the translation of the vibration region identified with SRF, from positive to negative C_m values, as κ is increased.

Without SRF, no vibration appears at $Re = 25$ for $\kappa = 0$. At $Re = 100$, the rectilinear responses present substantial magnitudes only for low $m_0^\star$, and their frequencies are restrained to a narrow range lower than St. An increase of κ results in the emergence of vibrations at $Re = 25$ and in an amplification of the responses, which exhibit substantial magnitudes over wider $m_0^\star$ intervals, and explore extended frequency ranges, roughly following the trend of f_n'. As for the system with SRF, the locked regime dominates the flow-body dynamics and the responses are overall close to sinusoidal. Occurrences of the unlocked regime at $Re = 100$ may, however, cause some slight deviations from harmonic evolutions (Bourguet 2023*a*).

The vibrations developing with and without SRF for $C_m < 0$ are almost identical at $Re = 25$ (figure 5). At $Re = 100$, some differences are expected due to possible deviations from sinusoidal oscillations, but the collapse of the responses appearing with and without SRF globally persists (figure 6). This indicates that the responses encountered with SRF can provide a reasonable *a priori* estimate of those arising without SRF. When the

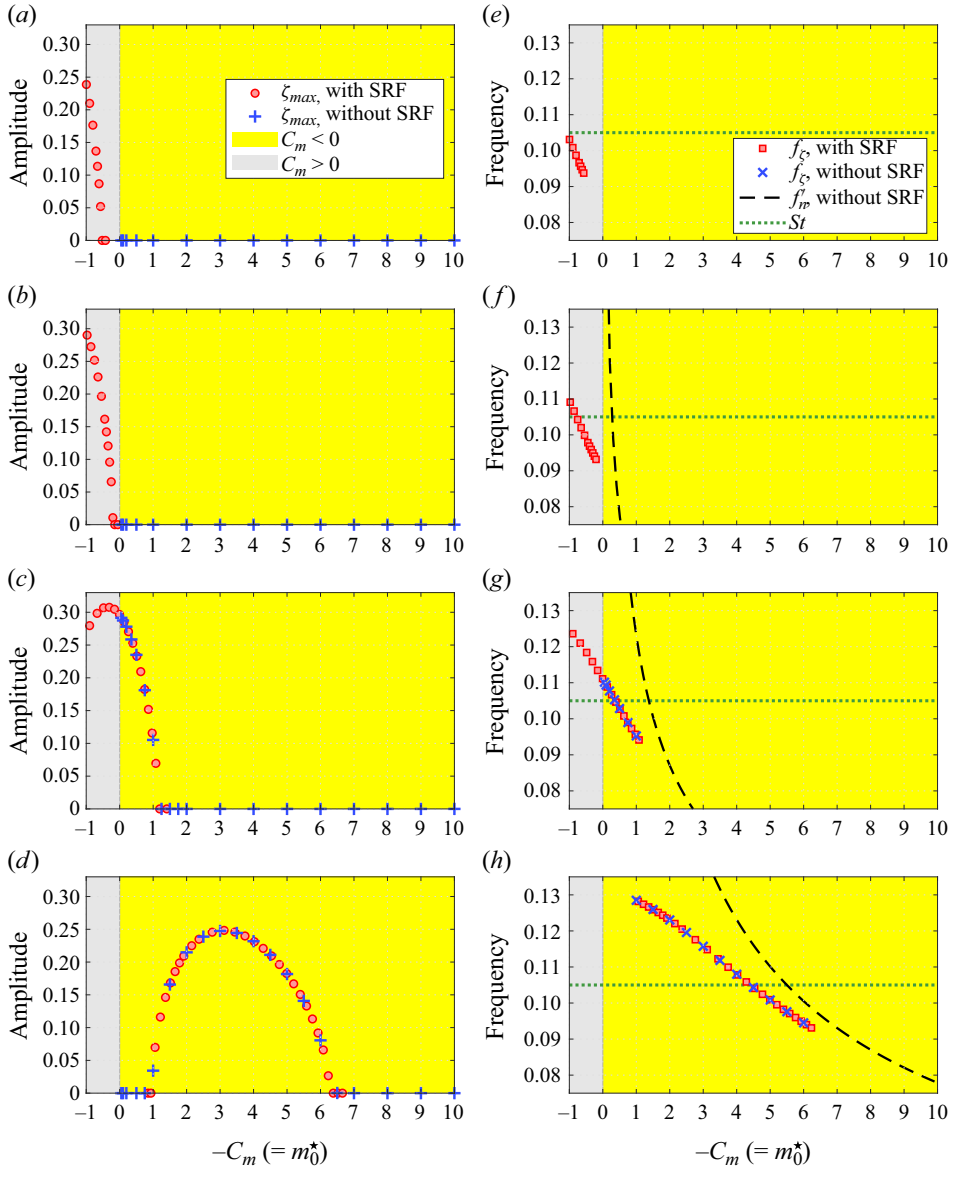

Figure 5. Displacement (*a–d*) amplitudes and (*e–h*) frequencies with and without SRF, as functions of $-C_m$, at $Re = 25$, for (*a*,*e*) $\kappa = 0$, (*b*,*f*) $\kappa = 0.1$, (*c*,*g*) $\kappa = 0.5$ and (*d*,*h*) $\kappa = 2$; without SRF, $-C_m = m_0^\star$. The displacement frequencies are plotted together with the modified natural frequency ((2.4) with $f_n = 0$) and St. Yellow and grey background colours denote the regions of negative and positive C_m, respectively.

vibration region observed with SRF moves towards negative C_m values, as κ is increased, all the responses with substantial amplitudes reached with SRF are progressively attained without SRF. Beyond a certain κ value, the presence or absence of SRF becomes nearly indiscernible. In other words, the behaviours of the systems with and without SRF, which clearly differ for $\kappa = 0$, tend to converge under the effect of path curvature.

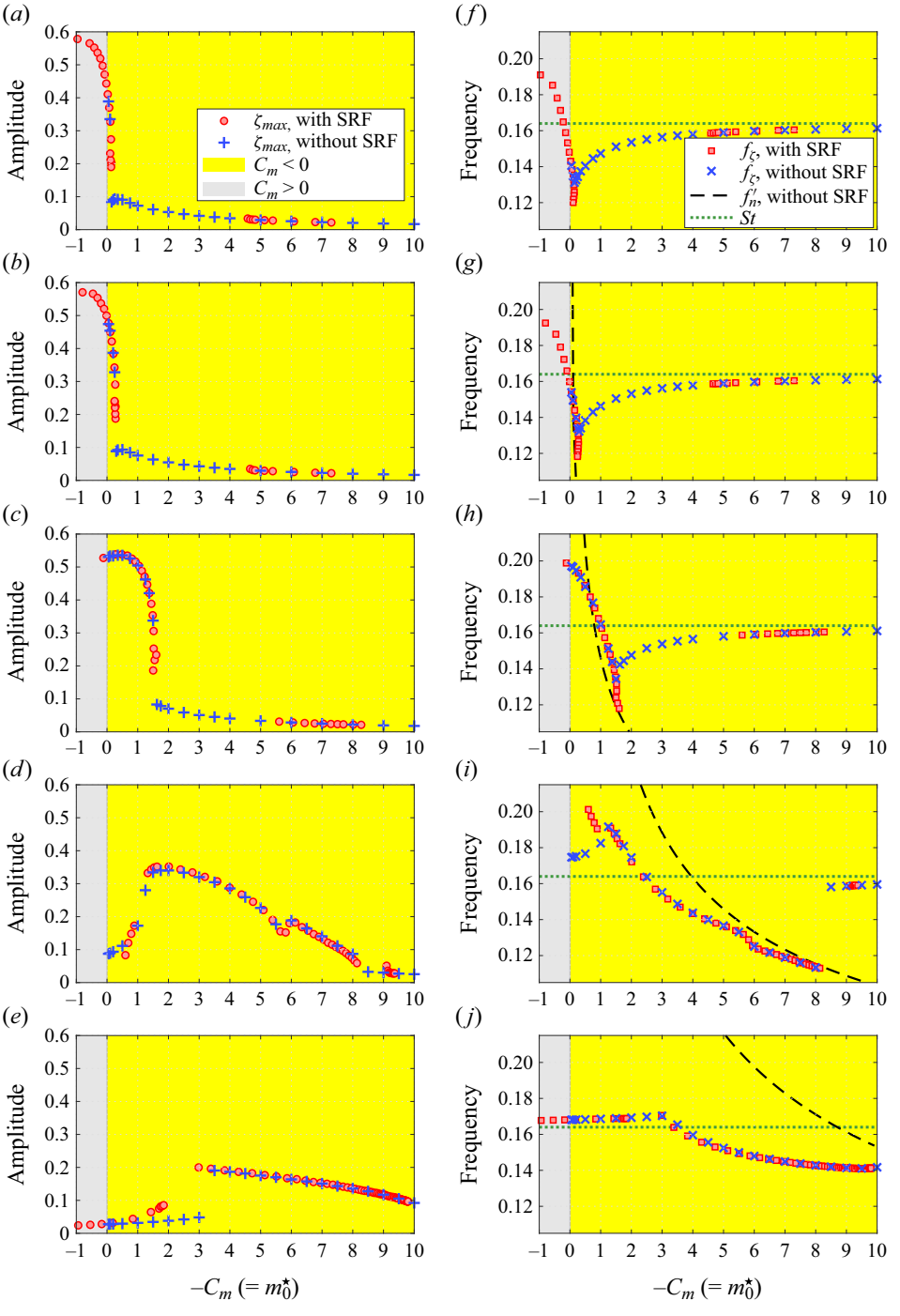

Figure 6. Same as figure 5 at $Re = 100$ for (a,f) $\kappa = 0$, (b,g) $\kappa = 0.1$, (c,h) $\kappa = 1$, (d,i) $\kappa = 5$ and (e,j) $\kappa = 11$.

4. Conclusions

The FIV of a cylinder with and without SRF have been examined with special attention paid to the influence of path curvature on their evolutions and possible connections. The study was conducted numerically for a cylinder, mounted on an elastic support or not, and free to translate along a circular path of variable radius, within a current at subcritical and postcritical Reynolds numbers, $Re = 25$ and $Re = 100$.

Under a harmonic oscillation assumption, the responses accessible without SRF correspond to those observed with SRF for which the effective added mass is negative. The actual vibrations issued from the simulations with and without SRF, and associated with negative C_m, globally collapse. Such a collapse is expected as the vibrations, which mainly develop through flow-body synchronization, and less frequently through a desynchronized regime, are generally close to sinusoidal. Along a transverse rectilinear path, i.e. the limiting case where path radius tends to infinity, most of the significant vibrations arising with SRF are characterized by positive C_m and thus *a priori* inaccessible without SRF. The simulated behaviours of the systems with and without SRF do indeed differ: vibrations occur with SRF but not without SRF at $Re = 25$, and the peak amplitudes reached with SRF at $Re = 100$ are not attained without SRF.

The principal result of this work is that the response ranges explored with and without SRF progressively converge as path curvature magnitude is increased. The simulations with SRF show that an increase of curvature magnitude causes a reduction of C_m, which indicates an expansion of the response range accessible without SRF. This expansion is confirmed by the simulations without SRF. It can be linked to the combined effects of the mean drag and path curvature, which tend to increase the ratio between the displacement and natural frequencies, or, equivalently, reduce C_m. The convergence of the system behaviours is accompanied by an enhancement of the responses appearing without SRF, as illustrated by the emergence of vibrations at $Re = 25$ and the widening of the mass-ratio intervals where significant responses develop. Beyond a certain curvature magnitude, all the significant vibrations encountered with SRF are also attained without SRF, and the presence or absence of SRF is virtually undetectable.

The similitude of the observations made at $Re = 25$ and $Re = 100$ reflects a continuity of the physical mechanisms at play between the subcritical- and postcritical-Re ranges. This suggests that the phenomena described here, in particular the convergence of the responses occurring with and without SRF, could persist at higher Re.

Acknowledgements. This work was performed using HPC resources from CALMIP (grants 2023-P1248 and 2024-P1248).

Funding. This research received no specific grant from any funding agency, commercial or not-for-profit sectors.

Declaration of interests. The author reports no conflict of interest.

Author ORCIDs.
Rémi Bourguet https://orcid.org/0000-0001-8079-3140.

References

BOURGUET, R. 2023*a* Path curvature enhances the flow-induced vibrations of a cylinder without structural restoring force. *J. Fluid Mech.* **977**, A31.

BOURGUET, R. 2023*b* Flow-induced vibrations of a cylinder along a circular arc. *J. Fluid Mech.* **954**, A7.

COSSU, C. & MORINO, L. 2000 On the instability of a spring-mounted circular cylinder in a viscous flow at low Reynolds numbers. *J. Fluids Struct.* **14**, 183–196.

DOLCI, D.I. & CARMO, B.S. 2019 Bifurcation analysis of the primary instability in the flow around a flexibly mounted circular cylinder. *J. Fluid Mech.* **880**, 1–11.

GOVARDHAN, R. & WILLIAMSON, C.H.K. 2002 Resonance forever: existence of a critical mass and an infinite regime of resonance in vortex-induced vibration. *J. Fluid Mech.* **473**, 147–166.

HOVER, F.S., TECHET, A.H. & TRIANTAFYLLOU, M.S. 1998 Forces on oscillating uniform and tapered cylinders in crossflow. *J. Fluid Mech.* **363**, 97–114.

KARNIADAKIS, G.E. & SHERWIN, S. 1999 *Spectral/HP Element Methods for CFD*, 1st edn. Oxford University Press.

KOU, J., ZHANG, W., LIU, Y. & LI, X. 2017 The lowest Reynolds number of vortex-induced vibrations. *Phys. Fluids* **29**, 041701.

NAVROSE & MITTAL, S. 2017 The critical mass phenomenon in vortex-induced vibration at low *Re*. *J. Fluid Mech.* **820**, 159–186.

NEWMAN, D.J. & KARNIADAKIS, G.E. 1997 A direct numerical simulation study of flow past a freely vibrating cable. *J. Fluid Mech.* **344**, 95–136.

PAÏDOUSSIS, M.P., PRICE, S.J. & DE LANGRE, E. 2010 *Fluid-Structure Interactions: Cross-Flow-Induced Instabilities*. Cambridge University Press.

RYAN, K., THOMPSON, M.C. & HOURIGAN, K. 2005 Variation in the critical mass ratio of a freely oscillating cylinder as a function of Reynolds number. *Phys. Fluids* **17**, 038106.

SHIELS, D., LEONARD, A. & ROSHKO, A. 2001 Flow-induced vibration of a circular cylinder at limiting structural parameters. *J. Fluids Struct.* **15**, 3–21.

SINGH, S.P. & MITTAL, S. 2005 Vortex-induced oscillations at low Reynolds numbers: hysteresis and vortex-shedding modes. *J. Fluids Struct.* **20**, 1085–1104.

WILLIAMSON, C.H.K. & GOVARDHAN, R. 2004 Vortex-induced vibrations. *Annu. Rev. Fluid Mech.* **36**, 413–455.

ZHANG, W., LI, X., YE, Z. & JIANG, Y. 2015 Mechanism of frequency lock-in in vortex-induced vibrations at low Reynolds numbers. *J. Fluid Mech.* **783**, 72–102.